Joint Rock Coefficient Estimation Based on Hausdorff Dimension

Dalibor Martišek

Institute of Mathematics, Faculty of Mechanical Engineering, Brno University of Technology, Brno, Czech Republic
Email: martisek@fme.vutbr.cz

Abstract

The strength of rock structures strongly depends inter alia on surface irregularities of rock joints. These irregularities are characterized by a coefficient of joint roughness. For its estimation, visual comparison is often used. This is rather a subjective method, therefore, fully computerized image recognition procedures were proposed. However, many of them contain imperfections, some of them even mathematical nonsenses and their application can be very dangerous in technical practice. In this paper, we recommend mathematically correct method of fully automatic estimation of the joint roughness coefficient. This method requires only the Barton profiles as a standard.

Keywords

Hausdorff Dimension, Self-Similarity, Self-Affinity, Box Counting Method, Power Function Method, Barton Profile, JRC Index

1. Introduction

A shape of geological discontinuities plays an important role in influencing the stability of rock masses. Many approaches have been used for its determination. The method of Barton and Choubey (1977) is well known in geotechnical practice. These authors introduced the method which is able to calculate the shear strength τ of rock joints as

$$\tau = \sigma_n \cdot \tan\left(\varphi_r + JRC \cdot \log \frac{JCS}{\sigma_n} \right) \tag{1}$$

where JRC is the joint roughness coefficient, JCS is the joint compressive strength, φ_r is the residual friction angle, and σ_n is the normal stress.

The method of Barton and Choubey [1] is well known in geotechnical prac-

tice-a visual comparison a fracture rock surface to be analysed with the standard Barton profiles is preferred way for determining *JRC* values.

A quick and easy estimate is probably one of the main reasons for this preference. However, this method is very subjective. Therefore, objective methods for *JRC* estimation are searched—see [2] [3] [4] [5] [6] for example. Unfortunately, some published papers contain many inaccuracies and even mathematical nonsenses. Application of some published "indicators of similarity" may be very dangerous in civil engineering. We refer to some of them and we recommend a mathematically correct method of fully automatic estimation of the *JRC* index in the following text.

2. Some Errors of Present Methods Based on Fractal Dimension

As was said in Introduction, subjective visual comparison a fracture rock surface to be analyzed with the standard Barton profiles (see **Figure 1**) is preferred way for determining *JRC* values. Objective methods for *JRC* are searched, unfortunately, many of them are incorrect.

Many researchers believe that the surface roughness of rock joints needs to be characterized using scale invariant parameters such as fractal parameters. Several researchers have suggested using the fractal dimension to quantify rock joint roughness (see [7]-[13] for example).

In [14], there is "derived" a "direct relationship" between the *JRC* index and fractal dimension D

$$JRC \approx 50 \cdot (D-1) \tag{2}$$

However, it is a nonsense as the following example illustrates.

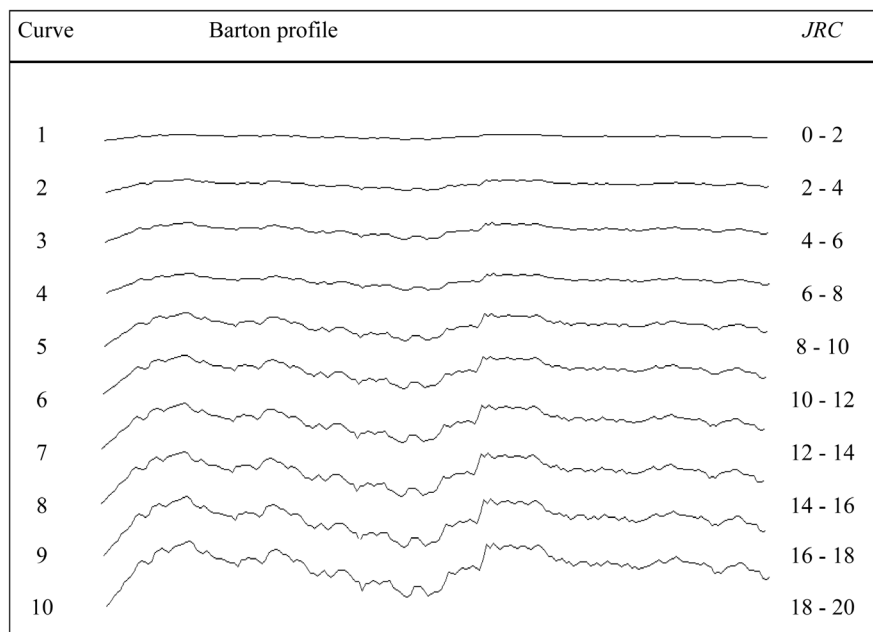| Curve	Barton profile	*JRC*
1		0 - 2
2		2 - 4
3		4 - 6
4		6 - 8
5		8 - 10
6		10 - 12
7		12 - 14
8		14 - 16
9		16 - 18
10		18 - 20

Figure 1. Standard Barton roughness profiles and their joint rock coefficients.

Example: A fractal dimension is namely affine invariant, *i.e.* each bijective affine transformation of the profile has the same dimension as an original. The profile $p(x)$ in **Figure 2** was generated as a fractional Brownian motion and for every x is $P(x) = 4 \cdot p(x)$. To easily determine the dimension of the resulting fractal, a random number must be generated by the Gaussian distribution $N(0;1)$ and the *i*-th iteration step variations σ_i have to be adjusted in accordance with

$$\sigma_i^2 = \frac{\sigma_0^2}{2^{2Hi}} \tag{3}$$

where $H \in \langle 0;1 \rangle$ is so called Hurst exponent.

Due to affine invariance, both profiles have the same dimension ($D = 1.5$) and should have the same roughness therefore. This is evidently not true. Moreover, *JRC* of both profiles is $JRC \approx 25$ according to (1). This is also not true.

In [14] [15], another „direct relationship" between dimension and *JRC* was published:

$$JRC = -0.87804 + 37.7844 \cdot \left(\frac{D-1}{0.015} \right) - 16.9304 \cdot \left(\frac{D-1}{0.015} \right)^2 \tag{4}$$

This relationship is often cited (see [16] [17] [18] [19] for example) but it is quite false. Equation (4) gives a totally nonsensical results for Barton profiles as will be shown in 2.5 (see the last column of **Table 3**).

Table 1. Hausdorff dimension and grid measure of the original Koch curve *A* and its affine representation *B* estimated by box-counting method and power-function method. Used affinity is $[x; y] \rightarrow [x; 2y]$.

|	Koch curve *A*				Koch curve *B*		
ε	N (ε)	ln(ε)	ln(p)	ε	N (ε)	ln(ε)	ln(p)
5	4322	1.6094	8.3715	5	32474	1.6094	10.3882
10	20449	2.3026	9.9257	10	13364	2.3026	9.5003
15	12296	2.7081	9.4170	15	7978	2.7081	8.9844
20	8701	2.9957	9.0712	20	5470	2.9957	8.6070
25	6512	3.2189	8.7814	25	4222	3.2189	8.3481
30	5201	3.4012	8.5566	30	3351	3.4012	8.1170
35	4250	3.5553	8.3547	35	2718	3.5553	7.9077
40	3585	3.6889	8.1845	40	2316	3.6889	7.7476
45	3049	3.8067	8.0226	45	2014	3.8067	7.6079
50	2674	3.9120	7.8913	50	1743	3.9120	7.4634
	Power. f.	Box-counting			Power. f.	Box-counting	
Dim.	**1.2621**		**1.2662**		**1.2627**		**1.2599**
Meas.	33365	exp (10.4184)	=33470		52739	exp (10.8730)	=52733

$$P(x) = 4 \cdot p(x)$$

$$p(x)$$
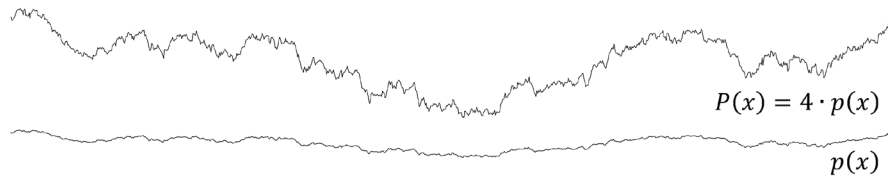
Figure 2. The profile $p(x)$ was generated as a fractional Brownian motion. Due to affine invariance, the profiles $p(x)$; $P(x)$ have the same dimension but evidently different roughness.

We can often read that for computing of fractal dimension, it is necessary to decide whether the object is self-similar or self-affine (see [20] [21] [22] [23]). It is said that "the computation of fractal dimensions of self-affine fractals requires modified computational methods" [14] [20] and their dimensions D have to be computed by others methods than the dimension of self-similar curves. Alleged reason is "different scaling" in the x-and y-directions which changes its dimensionality (see [14] for example). However, it is a deep mistake. One example for all: The curve B in **Figure 3** contains two its copies with the same scaling (red and pink). These copies required "non-modified" method. However, the same curve contains two copies with different scaling (green and blue). These copies required "modified" method. Can we use the modified or the non-modified method for its dimensionality estimation?

3. Hausdorff Measure and Hausdorff Dimension

Hausdorff defined the first dimension that allows non-integer values. Hausdorff s-dimensional outer measure of a set A is defined as

$$^{*}H^{(s)}(A) = \lim_{n \to \infty} \inf_{A \subseteq \bigcup A_{n;i}} \left\{ \sum_{i \in I} \left(diam\, A_{n;i} \right)^{s} \,\middle|\, diam\, A_{n;i} \leq \frac{1}{n} \right\} \tag{5}$$

where I is an at most countable index set. Restriction of $H^{(s)}$ to the sets measurable with $^{*}H^{(s)}$ (H-measurable sets) is called Hausdorff s-dimensional measure of the set A. The number

$$D_{H}(A) = \sup \left\{ d \in \mathbb{R}_{0}^{+} \bigcup \{\infty\} \,\middle|\, H^{(d)}(A) = \infty \right\} = \inf \left\{ d \in \mathbb{R}_{0}^{+} \bigcup \{\infty\} \,\middle|\, H^{(d)}(A) = 0 \right\} \tag{6}$$

is called Hausdorff dimension of the set A.

Mandelbrot [24] defined fractal as a set which Hausdorff dimension is sharply greater than the topologic dimension. Ever after several dimension which allows non-integer values was defined (see [25] for example). Each of them is called the fractal dimension.

For estimation of the Hausdorff dimension of sets which are constructed on digital devices, so called grid measure and grid dimension are used. The grid s-dimensional outer measure is defined as

$$^{*}G^{(s)}(A) = \lim_{n \to \infty} \inf_{A \subseteq \bigcup A_{n;i}} \left\{ \sum_{i \in I} \left(diam\, A_{n;i} \right)^{s} \,\middle|\, diam\, A_{n;i} = \frac{1}{n} \right\} \tag{7}$$
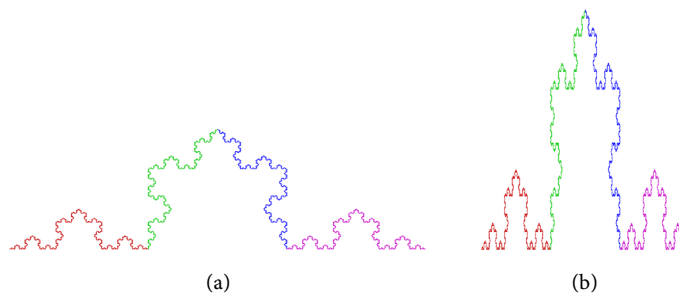
Figure 3. "Different scaling" in *x*- and *y*-directions can change the self-similar set (a) to self-affine set (b). However, "different scaling" in *x*- and *y*-directions can change the self-affine (b) to self-similar set (a).

Its restriction $G^{(s)}$ to the sets measurable with ${}^*G^{(s)}$ (*G*-measurable set) is called the grid measure. The grid dimension (*G*-dimension) of the set *A* is defined as

$$D_G(A) = \sup\left\{ d \in \mathbb{R}_0^+ \bigcup \{\infty\} \,\Big|\, G^{(d)}(A) = \infty \right\} = \inf\left\{ d \in \mathbb{R}_0^+ \bigcup \{\infty\} \,\Big|\, G^{(d)}(A) = 0 \right\} \quad (8)$$

The *G*-dimension is suitable for digital data and since the limit condition $n \to \infty$ in Formula (7) cannot be realized, the limit is omitted and the Formula (7) is replaced with the approximate equality

$$ {}^*G^{(s)}(A) \approx \inf_{A \subseteq \bigcup A_{n;i}} \left\{ \sum_{i \in I} \left(diam\, A_{n;i} \right)^s \,\bigg|\, diam\, A_{n;i} = \frac{1}{n} \right\} \quad (9)$$

4. Box Counting and Power-Function Method

For the infimum to be computed in (9), only those sets $A_{n;i}$ are taken to the union $\bigcup A_{n;i}$ for which $A_{n;i} \bigcap A \neq \varnothing$. Due to the fact that only bounded sets (or more precisely their approximations containing finite elements) can be represented in the computer, the system $\left\{ A_{n;i} \right\}$ is always finite. Let us denote its cardinality by $N(n)$. The measured approximations are always *G*-measurable. In software implementations of the measurement, used metric is a square metric, where the diameter of a square is equal to its side. According to Formula (9) we obtain for measure in Hausdorff dimension

$$ G^{(D)}(A) \approx \sum_{i=1}^{N(n)} \left(diam\, A_{n;i} \right)^D = \sum_{i=1}^{N(n)} \frac{1}{n^D} = N(n) \cdot n^{-D} \quad (10)$$

Therefore,

$$ N(n) \approx G^{(D)} \cdot n^D \quad (11)$$

Applying the logarithm on both sides of the approximate equality (11) we obtain

$$ \ln N(n) \approx D \cdot \ln n + \ln G^{(D)} \quad (12)$$

Measuring with a specified *n*, a $N(n)$ is obtained for a covering of the measured set. The values *D* and $G^{(D)}$ are calculated by fitting the straight line in the form (12) using the least square method. It is evident that for a high enough *n* we can calculate *D* as

$$D \approx \frac{\ln N(n)}{\ln n} \tag{13}$$

and even define the dimension as the limit of that fraction, *i.e.*

$$D_B = \lim_{n \to \infty} \frac{\ln N(n)}{\ln n} \tag{14}$$

This dimension and the method for its measurement are known as the box counting.

Note that n is the reciprocal value of the diameter of covering sets, which is often marked as ε. Therefore, if we denote the cardinality $N(n)$ of the covering of the set to be measured as $N(\varepsilon)$, we obtain

$$N(\varepsilon) \approx G^{(D)}(A) \cdot \varepsilon^{-D} \tag{15}$$

from (11)

$$\ln N(\varepsilon) \approx -D \cdot \ln \varepsilon + \ln G^{(D)}(A) \tag{16}$$

from (12) or

$$D_B = \lim_{\varepsilon \to 0+} \frac{\ln N(\varepsilon)}{\ln \varepsilon^{-1}} \tag{17}$$

from (14) respectively.

To calculate this dimension for the fractal *F*, it is necessary to insert this fractal into an evenly spaced grid and count how many squares (2D case) or boxes (3D case) are required to cover the set. The box-counting dimension is calculated by seeing how this number changes as we make the grid finer by applying a box-counting algorithm.

It is possible to shown that the theoretically defined box counting dimension (14) is equal to the Hausdorff dimension—see Formula (8). A problem is that the dimension (14) has to be estimated with the least-square method form the linear function (12). If we denote the power function (11) as $f(x) = G \cdot x^D$, sum of its residues is $R_n = \Sigma \left[N(n) - f(n) \right]^2$, while sum of residues for the linear function (12) is $R_n^* = \Sigma \left[\ln N(n) - \ln f(n) \right]^2$. Of course $R_n^* \ll R_n$. Thus the box-counting method systematically overestimates residues of low values and underestimates residues of its high values. Moreover, negative values of the difference $\ln N(n) - \ln f(n)$ have lower weights than positive values. This somehow lowers the tangent of the straight line as thus the value of the estimated dimension.

This problem can be overcome by searching for the power function (11) instead of the linear function (12). The least square method requires in this case minimization of the function

$$f(N, D) = \sum_n \left(N - G \cdot n^D \right)^2 \tag{18}$$

This leads to the equation

$$\sum_n \left(N n^D \ln n \right) \sum_n n^{2D} - \sum_n N n^D \sum_n \left(n^{2D} \ln n \right) = 0 \tag{19}$$

This equation is then solved numerically—see [26] for more information.

5. Self-Similarity and Self-Affinity

Many technical papers describe the fractals. We can read that the fractals can be either self-similar or self-affine and the original box counting method is a self-similar method and it provides accurate results only for self-similar profiles. Natural rock joint profiles are self-affine, therefore, the box-counting method is not useable for their fractal dimension—see [27] for example. However, these affirmations are very inaccurately. It is said that self-affine curves, in contrast to self-similar ones, are not identically scaled in *x*- and *y*-directions (see [14] [20] [21] [22] for example). This "definition" is unprofessional and very narrow (restricted). Many others fractals are self-affine.

A self-affine fractal is any fractal *F*, for which there exist affine mappings $\varphi_i; i = 1; 2; \cdots; n$ so it holds

$$F = \bigcup_{i=1}^{n} \varphi_i(F) = \bigcup_{i=1}^{n} F_i \tag{20}$$

If all affinities φ_i are the similarities then the self-affine fractal is concurrently self-similar. It means that the self-similarity is a special case of the self-affinity, *i.e.* each self-similar set is self-affine concurrently.

In Euclidean space, each affinity is given by

$$X' = \boldsymbol{F}_i \cdot X + \boldsymbol{v}_i \tag{21}$$

where $\boldsymbol{F}_i$ is any square matrix and $\boldsymbol{v}$ is any vector. If

$$\boldsymbol{F}_i \cdot \boldsymbol{F}_i^{\mathrm{T}} = \lambda^2 \cdot \boldsymbol{I} \tag{22}$$

(where $\boldsymbol{I}$ is the identity matrix) then the affinity is called the similarity, number λ is its coefficient. Except self-similar and self-affine fractals, there exist sets which are neither self-similar nor self-affine (Mandelbrot set for example).

According of the definition of the Hausdorff dimension is

$$0 < H^{(D)}(A) = \inf_{A \subseteq \bigcup_k A_{nk}} \left\{ \sum_{k \in I} \left(diam A_{n;i} \right)^s \middle| diam A_{n;i} \le \frac{1}{n} \right\} < \infty \tag{23}$$

If a set *A* is self-similar and $\lambda_1; \lambda_2; \cdots; \lambda_p$ are coefficients of the similarities φ_i from (20), and for each $i \ne j$ is $H^{(D)}\left(\varphi_i(A) \bigcap \varphi_j(A) \right) = 0$ then

$$H^{(D)}(A) = \inf_{A \subseteq \bigcup_k A_{nk}} \left\{ \sum_{k \in I} \left(diam A_{n;i} \right)^D \middle| diam A_{n;i} \le \frac{1}{n} \right\}$$

$$= \underbrace{\inf_{A \subseteq \bigcup_k A_{nk}} \left(diam A \right)^D}_{H^{(D)}(A)} \sum_{i=1}^{p} \lambda_i^D \tag{24}$$

It means that

$$H^{(D)}(A) = H^{(D)}(A) \cdot \sum_{i=1}^{p} \lambda_i^D \tag{25}$$

$$\lambda_1^D + \lambda_2^D + \cdots + \lambda_p^D = 1 \tag{26}$$

In case of $\lambda_1 = \lambda_2 = \cdots = \lambda_p = \lambda$ is

$$\lambda_1^D + \lambda_2^D + \cdots + \lambda_p^D = p \cdot \lambda^D = 1 \Rightarrow D = \frac{\ln p}{\ln \frac{1}{\lambda}} \qquad (27)$$

Example: the Koch curve is self-similar with four copies of itself, each scaled by the factor one third, its dimension is $D = \frac{\ln 4}{\ln 3}$. The Sierpinski triangle or Sierpinski square are also self-similar with three copies scaled by one half or eight copies scaled by one third respectively, their dimensions are $D = \frac{\ln 3}{\ln 2}$ or $D = \frac{\ln 8}{\ln 3}$ respectively.

For H-measure of any fractal, the H-measure of its covering $C = \bigcup_k A_{nk}$ is determinative. This covering consists of cubes in case of square metric. The measure of self-affine fractals (19) is equal to the sum of measures its affine copies φ_i. Each affinity φ_i transforms a cubical covering C to the set of parallelepipeds $\varphi_i(C)$. We have to find how the volume of cube will change by its transform to the parallelepiped.

Each cube is given by orthonormal vectors $\boldsymbol{a} = (a_1; a_2; a_3)$; $\boldsymbol{b} = (b_1; b_2; b_3)$; $\boldsymbol{c} = (c_1; c_2; c_3)$ which are transform to linearly independent vectors $\boldsymbol{a}' = (a_1'; a_2'; a_3')$; $\boldsymbol{b}' = (b_1'; b_2'; b_3')$; $\boldsymbol{c}' = (c_1'; c_2'; c_3')$ by bijective affinity φ_i, *i.e.*

$$\boldsymbol{a}'^{\mathrm{T}} = \boldsymbol{F}_i \cdot \boldsymbol{a}^{\mathrm{T}}; \quad \boldsymbol{b}'^{\mathrm{T}} = \boldsymbol{F}_i \cdot \boldsymbol{b}^{\mathrm{T}}; \quad \boldsymbol{c}'^{\mathrm{T}} = \boldsymbol{F}_i \cdot \boldsymbol{c}^{\mathrm{T}} \qquad (28)$$

or

$$\boldsymbol{a}' = \boldsymbol{a} \cdot \boldsymbol{F}_i^{\mathrm{T}}; \quad \boldsymbol{b}' = \boldsymbol{b} \cdot \boldsymbol{F}_i^{\mathrm{T}}; \quad \boldsymbol{c}' = \boldsymbol{F}_i^{\mathrm{T}} \cdot \boldsymbol{c}^{\mathrm{T}} \qquad (29)$$

where $\boldsymbol{F}_i$ is the matrix of the affinty φ_i. This implies

$$(a_1'; a_2'; a_3') = (a_1; a_2; a_3) \cdot \begin{pmatrix} z_{11} & z_{21} & z_{31} \\ z_{12} & z_{22} & z_{32} \\ z_{13} & z_{23} & z_{33} \end{pmatrix} = ((\boldsymbol{a}; \boldsymbol{f}_1); (\boldsymbol{a}; \boldsymbol{f}_2); (\boldsymbol{a}; \boldsymbol{f}_3)) \qquad (30)$$

By analogy

$$(b_1'; b_2'; b_3') = ((\boldsymbol{b}; \boldsymbol{f}_1); (\boldsymbol{b}; \boldsymbol{f}_2); (\boldsymbol{b}; \boldsymbol{f}_3)) \qquad (31)$$

$$(c_1'; c_2'; c_3') = ((\boldsymbol{c}; \boldsymbol{f}_1); (\boldsymbol{c}; \boldsymbol{f}_2); (\boldsymbol{c}; \boldsymbol{f}_3)) \qquad (32)$$

Volume of the parallelepiped which is given by vectors $\boldsymbol{a}'; \boldsymbol{b}'; \boldsymbol{c}'$ is equal to the scalar triple product. Therefore, we obtain

$$\begin{vmatrix} a_1' & a_2' & a_3' \\ b_1' & b_2' & b_3' \\ c_1' & c_2' & c_3' \end{vmatrix} = \begin{vmatrix} (\boldsymbol{a}; \boldsymbol{f}_1) & (\boldsymbol{a}; \boldsymbol{f}_2) & (\boldsymbol{a}; \boldsymbol{f}_3) \\ (\boldsymbol{b}; \boldsymbol{f}_1) & (\boldsymbol{b}; \boldsymbol{f}_2) & (\boldsymbol{b}; \boldsymbol{f}_3) \\ (\boldsymbol{c}; \boldsymbol{f}_1) & (\boldsymbol{c}; \boldsymbol{f}_2) & (\boldsymbol{c}; \boldsymbol{f}_3) \end{vmatrix}$$
$$= \begin{vmatrix} a_1 & a_2 & a_3 \\ b_1 & b_2 & b_3 \\ c_1 & c_2 & c_3 \end{vmatrix} \cdot \begin{vmatrix} f_{11} & f_{21} & f_{31} \\ f_{12} & f_{22} & f_{32} \\ f_{13} & f_{23} & f_{33} \end{vmatrix} \qquad (33)$$

from (30), (31), (32). Therefore

$$V(\boldsymbol{a}'; \boldsymbol{b}'; \boldsymbol{c}') = |\det \boldsymbol{F}_i^{\mathrm{T}}| \cdot V(\boldsymbol{a}; \boldsymbol{b}; \boldsymbol{c}) = |\det \boldsymbol{F}_i| \cdot V(\boldsymbol{a}; \boldsymbol{b}; \boldsymbol{c}) \qquad (34)$$

It is possible to obtain

$$S\left(\boldsymbol{a'};\boldsymbol{b'}\right) = \det \boldsymbol{F}_i \cdot S\left(\boldsymbol{a};\boldsymbol{b}\right)$$

for the area of the parallelogram in two-dimensional space. The diameter of cube (or square) which have the same volume (or area) in square metric is

$$\operatorname{diam} A'_{nk} = \sqrt[3]{\left|\det \boldsymbol{F}_i\right| \cdot V\left(\boldsymbol{a};\boldsymbol{b};\boldsymbol{c}\right)} = \sqrt[3]{\left|\det \boldsymbol{F}_i\right|} \cdot \operatorname{diam} A_{nk} \tag{35}$$

or

$$\operatorname{diam} A'_{nk} = \sqrt{\left|\det \boldsymbol{F}_i\right| \cdot S\left(\boldsymbol{a};\boldsymbol{b}\right)} = \sqrt{\left|\det \boldsymbol{F}_i\right|} \cdot \operatorname{diam} A_{nk} \tag{36}$$

respectively.

For the H-measure of a self-affine fractal A which contains p affine copies of itself, we obtain

$$
\begin{aligned}
H^{(D)}(A) &= \inf_{A \subseteq \bigcup_k A_{nk}} \left\{ \sum_{k \in I} \left(\operatorname{diam} A_{n;i}\right)^D \middle| \operatorname{diam} A_{nk} \le \frac{1}{n} \right\} \\
&= \inf_{A \subseteq \bigcup_k A_{nk}} \left\{ \sum_{k \in I} \left(\sqrt{\left|\det \boldsymbol{F}_i\right|} \cdot \operatorname{diam} A_{nk}\right)^D \middle| \operatorname{diam} A_{nk} \le \frac{1}{n} \right\} \\
&= \inf_{A \subseteq \bigcup_k A_{nk}} \left\{ \sum_{i=1}^{p} \left[\left(\sqrt{\left|\det \boldsymbol{F}_i\right|}\right)^D \sum_{k \in I} \left(\operatorname{diam} A_{nk}\right)^D \right] \middle| \operatorname{diam} A_{nk} \le \frac{1}{n} \right\} \\
&= \underbrace{\inf_{A \subseteq \bigcup_k A_{nk}} \sum_{k \in I} \left(\operatorname{diam} A_{nk}\right)^D}_{H^{(D)}(A)} \sum_{i=1}^{p} \left(\sqrt{\left|\det \boldsymbol{F}_i\right|}\right)^D \\
&= H^{(D)}(A) \sum_{i=1}^{p} \left(\sqrt{\left|\det \boldsymbol{F}_i\right|}\right)^D
\end{aligned}
$$

i.e.

$$H^{(D)}(A) = H^{(D)}(A) \sum_{i=1}^{p} \left(\sqrt{\left|\det \boldsymbol{F}_i\right|}\right)^D \tag{37}$$

Therefore

$$\sum_{i=1}^{p} \left(\sqrt{\left|\det \boldsymbol{F}_i\right|}\right)^D = 1 \tag{38}$$

and

$$\sum_{i=1}^{p} \left(\sqrt[3]{\left|\det \boldsymbol{F}_i\right|}\right)^D = 1 \tag{39}$$

in three-dimensional space by analogy.

6. Experiments with Approximations of Theoretical Sets

According to [27], the original box counting methods are the self-similar methods and they provide accurate results only for self-similar profiles. Problems are supposedly encountered when self-similar methods are used in the calculation of fractal dimensions for the self-affine objects. However, this is incorrect. The box counting method gives accurate or inaccurate results in case of self-similarity or self-affinity in the same way. However, the power function method does not suffer by any systematic error and is more precise as was said in the previous section.

Bijective affine transform (scaling in one direction for example) changes the measure of the transformed set but it does not change its dimensionality. For these measurement, the same methods may be used (without any modification). We estimated the dimensionality and measure of the Koch curve (see **Figure 3**), *i.e.* namely the self-similar original A and further its self-affine scaling $B:[x;y]\rightarrow[x;2y]$. The box counting method and power function method with the same parameters are used in both cases. Both curves have been generated as image with resolution 4096×4096 pixels. Results of these measurement are summarised in **Table 1** and graphically represented in **Figure 4** (box counting) and **Figure 5** (power function). For both curves (self-similar and self-affine), approximately the same dimension has been measured ($D\approx1.26$) using two methods (box counting and power function) with the same parameters ($\varepsilon=5,10,\cdots,50$) and withouth any modification. Theoretical dimension is $D=\dfrac{\ln4}{\ln3}=2.261859\cdots$ in both cases.

Straightlines (in case of the box counting) or power curves (in case of the power function) differs in shifting (extension) in vertical direction only. By this shifting (extension), set measure in corresponding fractal dimension is determined. Remind that the measure is the length in case of $D=1$ which is measured in linear micrometers (μm^1) for example. In case of $D=2$, the measure is caled the area which is measured in square micrometers (μm^2) for example. In case of Koch curve which dimension is $D=\dfrac{\ln4}{\ln3}$, we must measure in micrometers powered by $D=\dfrac{\ln4}{\ln3}$. If we presume that the pixel is a square with a side 1 μm then the measure of the curve A is
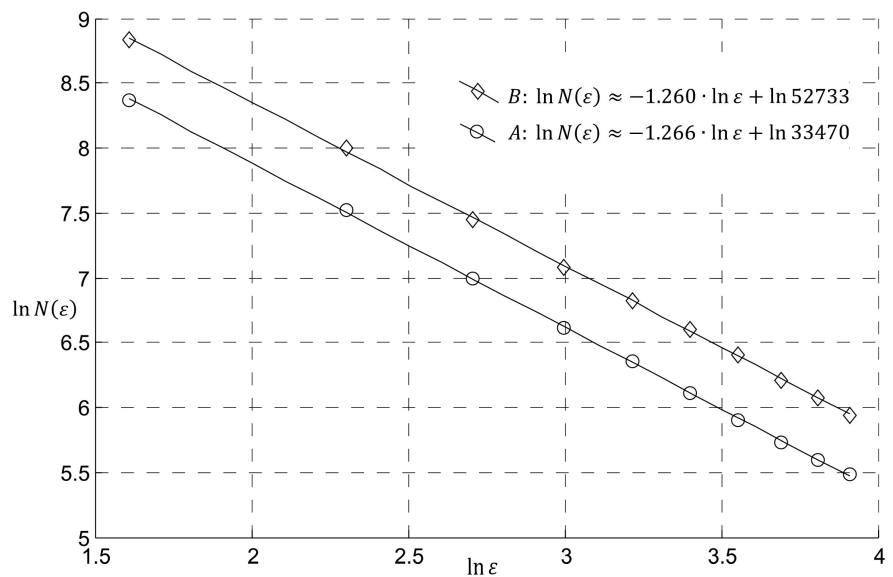

Figure 4. Box-counting dimension and box-counting measure of the Koch curve A and its affine representation B. Used affinity is $[x;y]\rightarrow[x;2y]$.
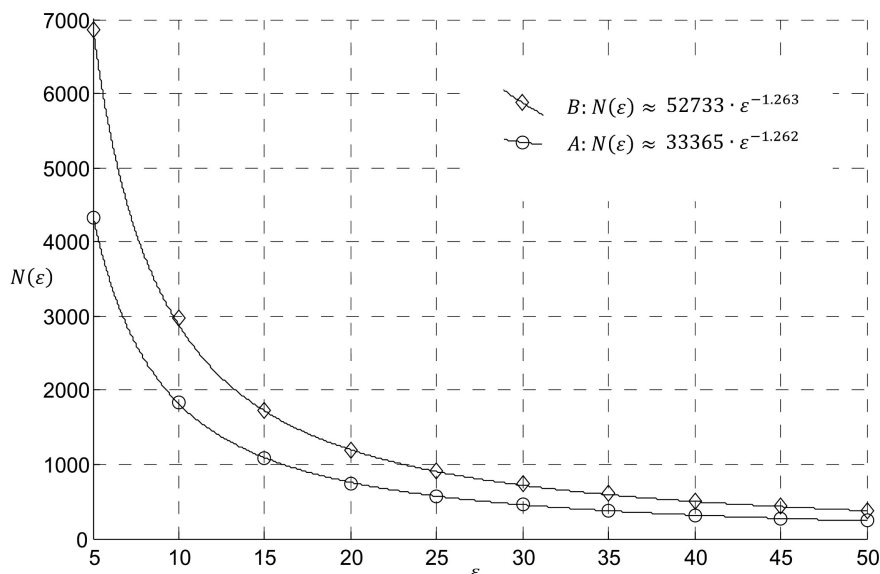
Figure 5. Hausdorff dimension and grid measure of the Koch curve *A* and its affine representation *B*. Power-function method, used affinity is $[x; y] \rightarrow [x; 2y]$.

$$G^{(D)}(A) \approx \exp(10.4184) \approx 33470 \, \mu\text{m}^D \qquad (40)$$

according to box counting method and

$$G^{(D)}(A) \approx 33365 \, \mu\text{m}^D \qquad (41)$$

according to power function method. For the affine representation *B* of the curve *A*, these values are

$$G^{(D)}(B) \approx \exp(10.8730) \approx 52733 \, \mu\text{m}^D \qquad (42)$$

according to box counting method and

$$G^{(D)}(B) \approx 52739 \, \mu\text{m}^D \qquad (43)$$

according to power function method.

For testing of the power function method, following fractals has been chosen: Koch curve, Sierpinski triangle and Sierpinski square (see previous example). The subsequent set (triangle) is constructed as the union of three affine copies of itself, matrices of the affinities—see Equation (21)—are

$$\boldsymbol{F}_1 = \begin{pmatrix} 0.36 & 0.48 \\ 0.48 & -0.36 \end{pmatrix}; \; \boldsymbol{F}_2 = \begin{pmatrix} 0.36 & -0.48 \\ -0.48 & -0.36 \end{pmatrix}; \; \boldsymbol{F}_3 = \begin{pmatrix} -0.28 & 0 \\ 0 & 0.28 \end{pmatrix} \qquad (44)$$

(vectors $\boldsymbol{v}_i$ are irrelevant for its dimension) then it implies from (38)

$$\left(\sqrt{|\det \boldsymbol{F}_1|} \right)^D + \left(\sqrt{|\det \boldsymbol{F}_2|} \right)^D + \left(\sqrt{|\det \boldsymbol{F}_3|} \right)^D = 1 \qquad (45)$$

in our case

$$\left(\sqrt{0.36} \right)^D + \left(\sqrt{0.36} \right)^D + \left(\sqrt{0.0784} \right)^D = 1 \qquad (46)$$

and $D = 1.622339\cdots$

This triangle is self-affine, however it also holds

$$\boldsymbol{F}_1\boldsymbol{F}_1^{\mathrm{T}} = \boldsymbol{F}_2\boldsymbol{F}_2^{\mathrm{T}} = 0.6^2 \cdot \boldsymbol{I}; \; \boldsymbol{F}_3\boldsymbol{F}_3^{\mathrm{T}} = 0.28^2 \cdot \boldsymbol{I} \tag{47}$$

It means that this fractal is not only self-affine but also self-similar. It consists of two contractions with $\lambda_1 = \lambda_2 = 0.36$ and one contraction with $\lambda_3 = 0.28$. Therefore, we can also use Equation (26)

$$0.6^D + 0.6^D + 0.28^D = 1 \tag{48}$$

It is the same equation as (46) and gives the same result. This fractal is illustrated in Figure 6 on the left and it is called "subsequent triangle" in Table 2.

As the next fractal, a self-affine set is constructed (see Figure 6 on the right, it is named as "self-affine square" in Table 2). It contains five affine copies of itself, matrices of the affinities are

$$\boldsymbol{F}_1 = \boldsymbol{F}_2 = \boldsymbol{F}_3 = \boldsymbol{F}_4 = \boldsymbol{F}_5 = \begin{pmatrix} \dfrac{1}{3} & 0 \\ 0 & \dfrac{1}{2} \end{pmatrix} \tag{49}$$
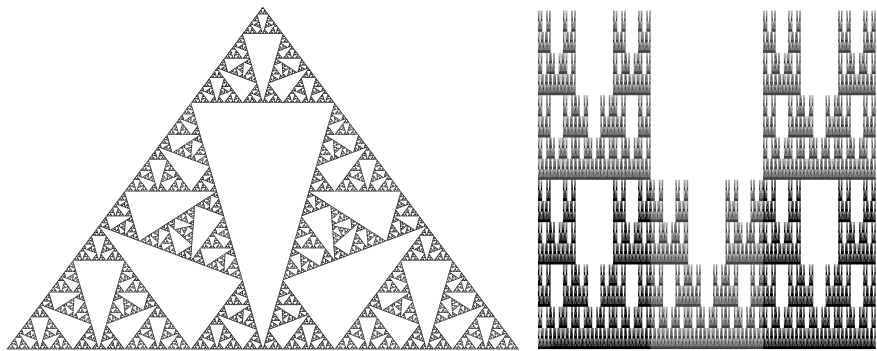

Figure 6. The self-affine triangle and self-affine square.

Table 2. The theoretical dimension of some self-similar and self-affine fractals and the dimension estimated by the power function method.

	self-	theoretical	Dimension estimated	error (%)
Koch curve	-similary	$\dfrac{\ln 4}{\ln 3} \approx 1.26185$	1.26377	0.152
Sierpinski triangle	-similary	$\dfrac{\ln 3}{\ln 2} \approx 1.58496$	1.58466	0.019
Sierpinski square	-similary	$\dfrac{\ln 8}{\ln 3} \approx 1.89279$	1.88729	0.291
Subsequent triangle	-similary	1.62234	1.62342	0.067
Self-affine square	-affine	1.79649	1.79134	0.287
Barnsley fern	-affine	1.76462	1.76249	0.121
Tree	-affine	1.81616	1.80511	0.612
Sea horse	-affine	1.79616	1.78110	0.846

its dimension is

$$\sum_{i=1}^{5}\left(\sqrt{|\det \boldsymbol{M}_i|}\right)^D = 1 \Rightarrow 5 \cdot \left(\sqrt{\frac{1}{6}}\right)^D = 1 \Rightarrow D = 2 \cdot \frac{\ln 5}{\ln 6} \approx 1.796488 \cdots \qquad (50)$$

Sixth set in Table 2 is the Barnsley fern (see Figure 7 on the left), it has the affinity matrices

$$\boldsymbol{F}_1 = \begin{pmatrix} 0.01 & 0 \\ 0 & 0.2 \end{pmatrix}; \boldsymbol{F}_2 = \begin{pmatrix} 0.2 & 0.2 \\ -0.3 & 0.2 \end{pmatrix}; \boldsymbol{F}_3 = \begin{pmatrix} -0.1 & 0.3 \\ 0.3 & 0.2 \end{pmatrix}; \boldsymbol{F}_4 = \begin{pmatrix} 0.83 & -0.05 \\ 0.05 & 0.83 \end{pmatrix} \qquad (51)$$

According to (37) its dimension is $D = 1.764625 \cdots$

Seventh tested fractal is a tree (see Figure 7 in the middle) with matrices

$$\boldsymbol{F}_1 = \begin{pmatrix} 0.195 & -0.488 \\ 0.344 & 0.443 \end{pmatrix}; \ \boldsymbol{F}_2 = \begin{pmatrix} 0.462 & 0.414 \\ -0.252 & 0.361 \end{pmatrix};$$

$$\boldsymbol{F}_3 = \begin{pmatrix} -0.058 & -0.070 \\ 0.453 & -0.111 \end{pmatrix}; \ \boldsymbol{F}_4 = \begin{pmatrix} -0.637 & 0 \\ 0 & 0.501 \end{pmatrix} \qquad (52)$$

and dimension $D = 1.816162 \cdots$

The last fractal-"sea horse" has matrices

$$\boldsymbol{F}_1 = \begin{pmatrix} 0.8 & 0.3 \\ -0.3 & 0.8 \end{pmatrix}; \ \boldsymbol{F}_2 = \begin{pmatrix} -0.3 & 0.3 \\ -0.4 & -0.3 \end{pmatrix} \qquad (53)$$

and dimension $D = 1.796166 \cdots$ (see Figure 7 on the right).

In Table 2, we can compare these theoretical dimensions of previous eight sets with the dimension which was estimated by the power function method. Data was generated by the IFS method (original resolution 4096×4096 pixels). It is clear that the results of this method are sufficiently precise for both types of fractals.

7. Estimation of Hausdorff Dimension of Barton Profiles

Some authors alerts, that any fractal dimension itself cannot be used for roughness modelling (see [7] [28] [29] [30] for example). It is also clear from the example in Section 2 and from Figure 2. We illustrate this fact also in the case of the Barton Profile.
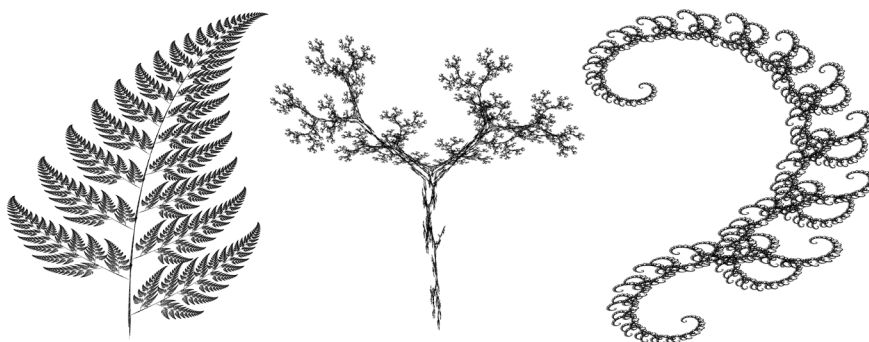

Figure 7. The self-affine fractals—fern, tree and sea horse.

In **Figure 8**, we can see the original of fourth Barton profile (K) and its scalings $L:[x;y] \rightarrow [x;5y]$; $M:[x;y] \rightarrow [x;10y]$. These three profiles have been measured by the power function method with the same parameters.

These measurement are graphically represented in **Figure 9**. For all three profiles, approximately the same dimension has been measured.

8. *JRC* Estimators

As is clear from previous text, *JRC* depends not only on the fractal dimension, but also on its statistical variability. Remember that the important variability characteristics are:

The square root of average of the squared differences from the mean, *i.e.*

$$\sigma(n) = \sqrt{\frac{1}{n}\sum_{i=1}^{n}(x_i - \overline{x})^2} \tag{54}$$

where n is the number of elements of the set, x_i are its elements and $\overline{x}$ is arithmetic mean (standard deviation) and the arithmetic mean of absolute values of differences between elements of statistical sets and their arithmetic mean, *i.e.*

$$\rho(n) = \frac{1}{n}\sum_{i=1}^{n}|x_i - \overline{x}| \tag{55}$$

original (K) $L:[x;y] \rightarrow [x;5y]$ $M:[x;y] \rightarrow [x;10y]$
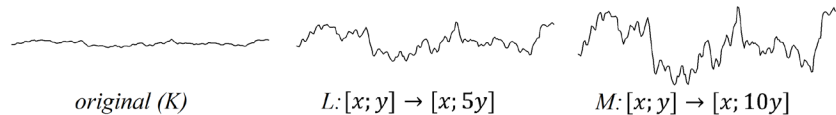
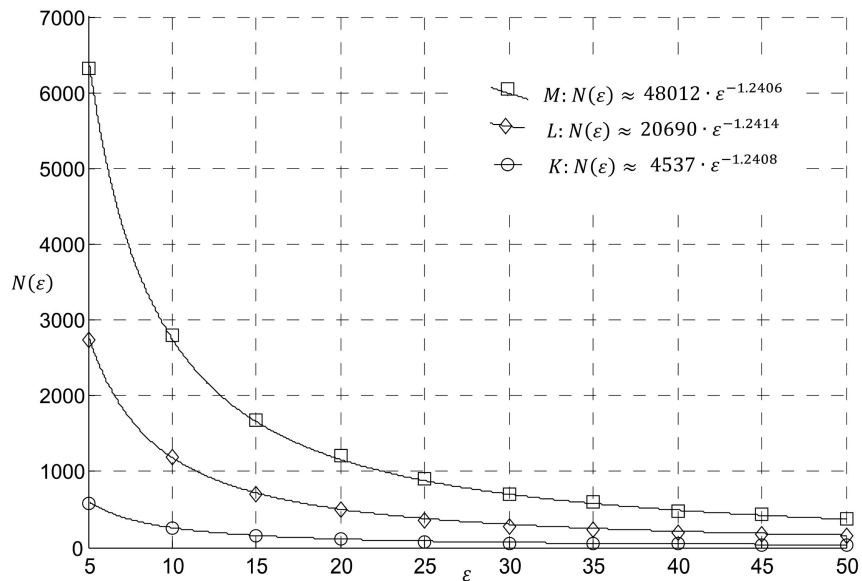**Figure 8.** The fourth Barton profile and its affine copies.

Figure 9. Hausdorff dimension and grid measures of the fourth Barton profile (K) and its affine representations K, M. Power-function method, used affinities are $[x;y] \rightarrow [x;5y]$ or $[x;y] \rightarrow [x;10y]$ respectively.

(average deviation).

The Hurst exponent is directly related to the fractal dimension, which measures the smoothness of a surface, or, in our case, the smoothness of a rock profiles. The relationship between the fractal dimension D and the Hurst exponent H, is given by

$$H = n + 1 - D \tag{56}$$

where n is the topological dimension of the measured set (see (59) for example). The Equation (56)—see [31] or [32] for proof—enables to compare the roughness in different topological dimensions and also to compare the standard Barton $2D$ profile with the real $3D$ profiles to be measured. Therefore, a roughness estimator can be designed to be able to determine the JRC in different topological dimensions, *i.e.* the JRC of fractal curves and the JRC of fractal surfaces as well. Therefore, it works with the Hurst exponent for which values is $H \in \langle 0;1 \rangle$ in both cases instead the fractal dimension for which is $D \in \langle 1;2 \rangle$ in case of the fractal curves and $D \in \langle 2;3 \rangle$ in case of the fractal surfaces.

The JRC is given not only by the Hurst exponent but also by heights of curve or surface irregularities. These irregularities can be quantified using the standard deviation (54) or average deviation (55).

Increasing irregularities heights denotes increasing of the JRC and conversely. Therefore, the standard deviation (53) or average deviation (55) must be placed to numerator of expression to be found. Thus, corresponding formulas are:

$$E_\sigma = \frac{\sigma}{H} \tag{57}$$

(standard deviation estimator)

$$E_\rho = \frac{\rho}{H} \tag{58}$$

(average deviation estimator), σ and ρ are given by (54), (55).

For JRC estimation of any profile or surface, so called characteristic functions $JRC_\sigma(E_\sigma)$; and $JRC_\rho(E_\rho)$ have been constructed. Each of them has been designed to pass through the origin of the coordinate system (if surface variability is equal to zero then surface is completely smooth horizontal plane, Hurst exponent is equal to one and $JRC = 0$). Each of them must be non-negative and increasing (as the JRC). Each of them must describe a dependence of the JRC on E_σ or E_ρ respectively and has been found using of the least squares method.

9. Estimation of the Characteristic Functions

In this section, Hausdorff dimension of all standard Barton profiles has been estimated using power function method and values of E_σ; E_ρ for the standard Barton profiles have been measured. Results of these measurements are summarized in Table 3.

For JRC estimation of any profile or surface, so called characteristic functions $JRC_\sigma(E_\sigma)$; and $JRC_\rho(E_\rho)$ have been constructed. Each of them has been de-

Table 3. Hausdorff dimensions, Hurst exponents, standard deviations, average deviations, standard deviation estimators and average deviation estimators of the standard Barton profiles. In the last column, "*JRC*" assigned to corresponding dimension by present used and often cited expression (4).

No	Dim	Hurst	σ	ρ	E_σ	E_ρ	JRC	JRC (2)
1	1.023	0.977	0.081	0.030	0.083	0.031	1	17.253
2	1.147	0.853	0.159	0.124	0.187	0.146	3	−1256.586
3	1.192	0.808	0.334	0.272	0.414	0.337	5	−2291.114
4	1.241	0.759	0.498	0.397	0.656	0.524	7	−3764.184
5	1.286	0.714	0.646	0.552	0.904	0.773	9	−5435.295
6	1.314	0.686	0.894	0.760	1.303	1.108	11	−6628.901
7	1.335	0.665	1.134	0.933	1.705	1.403	13	−7601.534
8	1.357	0.643	1.416	1.186	2.202	1.844	15	−8691.665
9	1.365	0.635	1.641	1.460	2.585	2.299	17	−9106.136
10	1.398	0.602	1.910	1.693	3.172	2.813	19	−10917.635

signed to pass through the origin of the coordinate system (if surface variability is equal to zero then surface is completely smooth horizontal plane, Hurst exponent is equal to one and $JRC = 0$). Each of them must be non-negative and increasing (as the *JRC*). Each of them must describe a dependence of the *JRC* on E_σ or E_ρ respectively and has been found using of the least squares method.

Equations of these functions are

$$JRC_\sigma \left(E_\sigma \right) = 9.186 \cdot E_\sigma^{0.651} \tag{59}$$

(see **Figure 10**)

$$JRC_\rho \left(E_\rho \right) = 10.095 \cdot E_\rho^{0.612} \tag{60}$$

(see **Figure 11**).

10. Estimation of the *JRC* Index of Real Samples

All geological data used in this paper has been acquired by prof. Tomáš Ficker from the Faculty of Civil Engineering of our university. All the samples are specimens of limestone (locality Brno-Hády, Czech Republic). All processing and visualization of these data have been made by original author's software. For more information of these reconstructions and visualizations see [33] [34] [35] [36].

In this section, limestone surfaces in **Figure 12** have been used for testing.

If we presume that the surface is isotropic, *i.e.* its joint roughness coefficient is not dependent on the direction, one *JRC* may be assigned to $3D$ surface. In this case, the surface is covered by diminishing cubes (thickening spatial grid) for estimation of the Hausdorff dimension using power function method according to (21). There is $D \in \left(2;3 \right)$, $n = 3$ and $H \in \left(0;1 \right)$ in expression (56) which serves for *JRC* estimation. This *JRC* we call the global *JRC*.
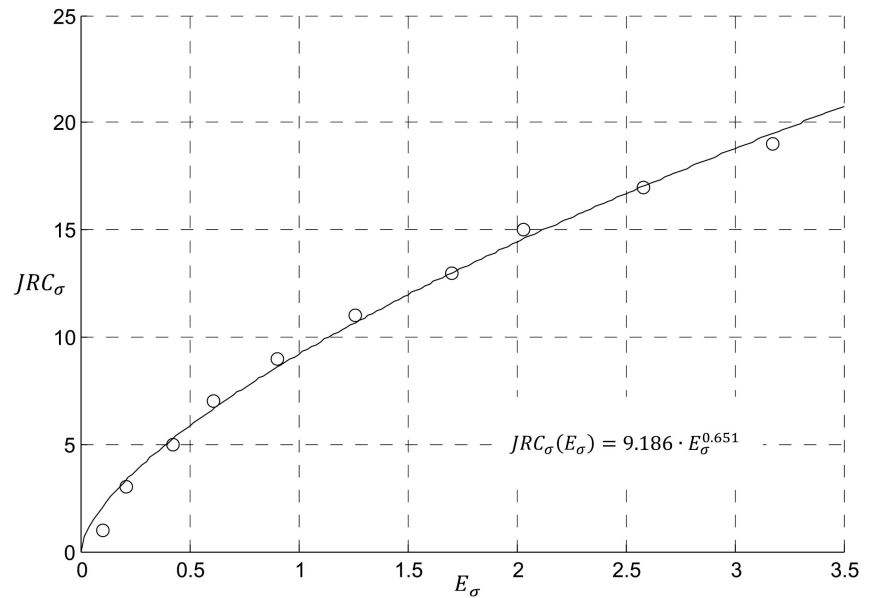
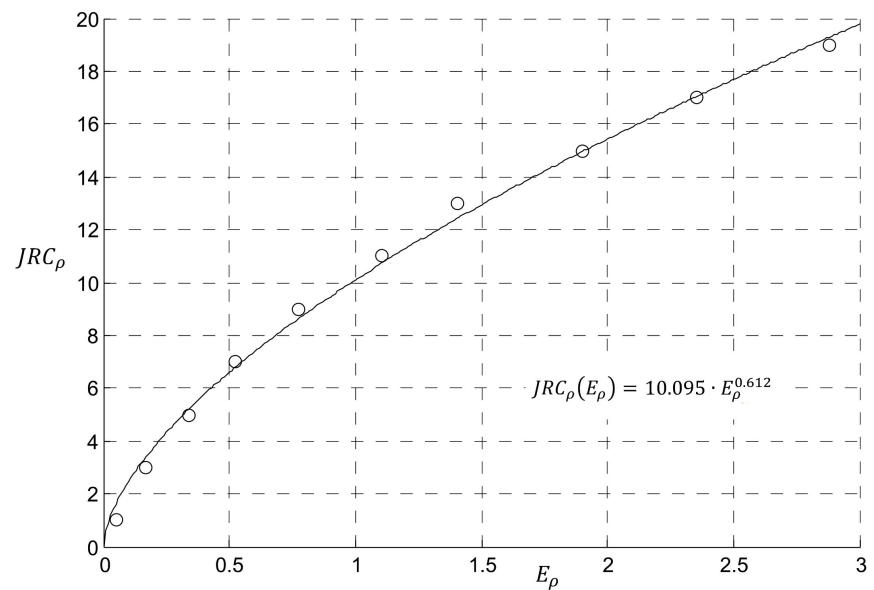**Figure 10.** The *JRC* as function of standard deviation estimator E_σ —see (59).

$$JRC_\sigma(E_\sigma) = 9.186 \cdot E_\sigma^{0.651}$$

Figure 11. The *JRC* as function of average deviation estimator E_ρ —see (60).

$$JRC_\rho(E_\rho) = 10.095 \cdot E_\rho^{0.612}$$

However, the *JRC* may have different values along different orientations on a rock surface. In this case, we can choose the direction of the *JRC* estimation. The profile curve is generated for selected direction and its Hausdorff dimension is measured by power function method according to (11). There is $D \in (1;2)$, $n = 2$ in expression (56) and also $H \in (0;1)$ in expressions (57), (58) which serves for *JRC* estimation. This *JRC* we call the directional *JRC*.

The global *JRC* has been estimated for the samples $A;B;C;D$ from **Figure 12**. For each of them, thirty six directions have been chosen for estimation of the directional *JRC*. These directions are illustrated in **Figure 13** for the sample *D*.
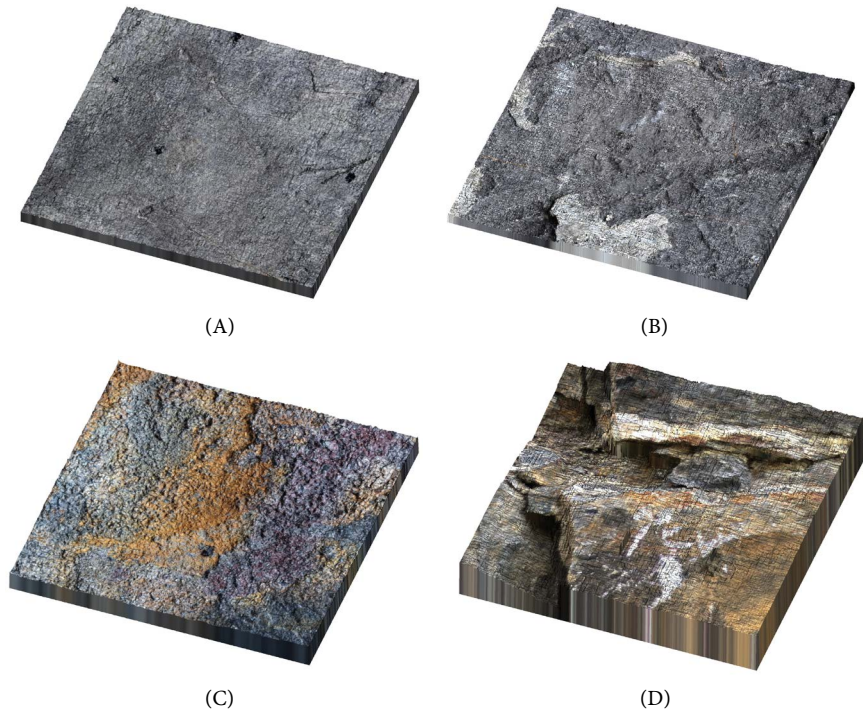
(A)

(B)

(C)

(D)

Figure 12. The limestone samples under tests. $3D$ reconstruction from the series of partially focused images (see [33] [34] [35] [36] for more information).
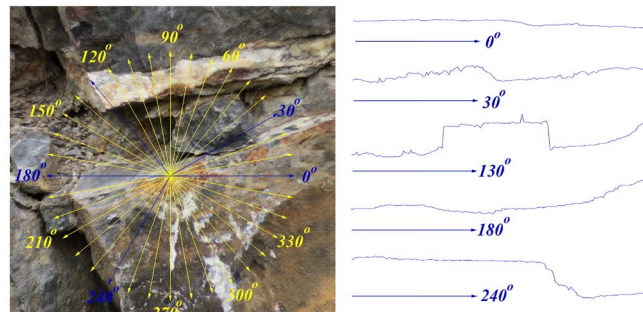

Figure 13. Directions that were used for estimation of the directional *JRCs* of the samples $A; B; C; D$. The profiles marked as blue on the left are illustrated on the right.

Results of these measurements are summarized in **Table 4** and **Table 5** and graphically represented in **Figures 14-19**. In **Figure 14** we can see dimension estimation of the profile with direction 0° on the sample A, the profile with direction 90° on the sample B, the profile with direction 100° on the sample C and the profile with direction 200° on the sample D using box counting method. In **Figure 15**, there are illustrated estimation of the same profiles using power function method.

In the second last row of **Table 2** and **Table 3**, averages of Hausdorff dimensions, Hurst exponents, standard deviations, average deviations and *JRCs* in individual directions are stated. In the last row of **Table 4** and **Table 5**, the Hausdorff dimension, Hurst exponent, standard deviation, average deviation and *JRCs* measured over the whole surface are stated. In **Figures 16-19**.

Table 4. Hausdorff dimensions estimated by power function method, Hurst exponents, standard deviations, average deviations and directional *JRCs* of the samples A, B. Averaged values on these quantities are in the second last row, corresponding values of the global *JRCs* are in the last row.

Angle	Sample A						Sample B					
	Dim	Hurst	σ	ρ	JRC_σ	JRC_ρ	Dim	Hurst	σ	ρ	JRC_σ	JRC_ρ
0°	1.330	0.670	1.028	1.076	5.523	5.481	1.280	0.720	1.405	1.519	6.450	6.464
10°	1.381	0.619	0.960	1.037	5.560	5.620	1.269	0.731	1.484	1.543	6.622	6.469
20°	1.448	0.552	0.934	0.989	5.886	5.856	1.195	0.805	1.706	1.854	6.806	6.818
30°	1.395	0.605	0.914	0.971	5.468	5.479	1.250	0.750	1.894	2.040	7.630	7.545
40°	1.373	0.627	0.808	0.869	4.931	5.011	1.250	0.750	1.893	2.133	7.624	7.751
50°	1.403	0.597	0.698	0.668	4.632	4.403	1.237	0.763	1.480	1.941	6.425	7.242
60°	1.337	0.663	0.656	0.650	4.156	4.060	1.262	0.738	1.348	1.586	6.183	6.539
70°	1.316	0.684	0.551	0.538	3.638	3,553	1.250	0.750	1.141	1.328	5.492	5.814
80°	1.218	0.782	0.584	0.562	3.463	3.363	1.214	0.786	1.385	1.416	6.040	5.875
90°	1.277	0.723	0.603	0.556	3.722	3.504	1.268	0.732	1.141	1.204	5.577	5.558
100°	1.448	0.552	0.505	0.502	3.951	3.879	1.299	0.701	0.807	1.255	4.586	5.854
110°	1.367	0.633	0.581	0.604	3.959	3.996	1.264	0.736	0.775	1.303	4.328	5.813
120°	1.376	0.624	0.613	0.694	4.139	4.385	1.381	0.619	0.803	1.063	4.954	5.708
130°	1.260	0.740	0.918	0.914	4.811	4.674	1.262	0.738	0.838	1.262	4.546	5.692
140°	1.289	0.711	1.074	1.081	5.466	5.299	1.466	0.534	0.936	1.066	6.018	6.252
150°	1.262	0.738	1.211	1.231	5.768	5.607	1.313	0.687	1.248	1.322	6.163	6.114
160°	1.296	0.704	1.213	1.212	5.952	5.713	1.350	0.650	1.522	1.500	7.265	6.828
170°	1.244	0.756	1.202	1.214	5.651	5.479	1.316	0.684	1.620	1.705	7.314	7.152
180°	1.306	0.694	1.036	0.983	5.424	5.075	1.268	0.732	2.141	2.344	8.385	8.327
190°	1.286	0.714	0.933	0.915	4.974	4.775	1.334	0.666	2.241	2.427	9.189	9.012
200°	1.279	0.721	0.930	0.868	4.934	4.601	1.249	0.751	2.541	2.683	9.220	8.903
210°	1.246	0.754	0.889	0.828	4.653	4.349	1.233	0.767	2.777	2.902	9.629	9.213
220°	1.283	0.717	0.717	0.708	4.185	4.079	1.143	0.857	3.139	3.692	9.701	9.970
230°	1.334	0.666	0.669	0.600	4.196	3.858	1.141	0.859	3.653	4.028	10.689	10.498
240°	1.305	0.695	0.576	0.554	3.705	3.580	1.066	0.934	4.256	4.565	11.179	10.766
250°	1.326	0.674	0.541	0.510	3.629	3.470	1.184	0.816	4.395	4.850	12.460	12.124
260°	1.291	0.709	0.474	0.443	3.222	3.090	1.084	0.916	4.730	5.288	12.126	11.913
270°	1.273	0.727	0.488	0.434	3.234	3.006	1.179	0.821	4.651	5.155	12.878	12.538
280°	1.368	0.632	0.480	0.426	3.500	3.234	1.107	0.893	4.713	5.053	12.296	11.768
290°	1.350	0.650	0.511	0.474	3.581	3.393	1.094	0.906	4.410	4.679	11.664	11.130
300°	1.350	0.650	0.541	0.525	3.715	3.610	1.180	0.820	4.010	4.349	11.708	11.318
310°	1.348	0.652	0.631	0.636	4.098	4.048	1.116	0.884	3.858	4.270	10.871	10.690
320°	1.359	0.641	0.684	0.673	4.364	4.232	1.124	0.876	3.633	4.060	10.521	10.428
330°	1.320	0.680	0.819	0.781	4.723	4.471	1.165	0.835	3.412	3.833	10.421	10.367
340°	1.351	0.649	0.879	0.868	5.092	4.903	1.218	0.782	2.421	2.281	8.700	7.867
350°	1.340	0.660	0.998	0.996	5.471	5.276	1.280	0.720	1.418	1.804	6.491	7.177
Aver.	1.326	0.674	0.774	0.766	4.538	4.400	1.228	0.772	2.441	2.720	8.370	8.424
3D	2.312	0.688	0.783	0.761	4.549	4.369	2.205	0.795	2.349	2.468	8.443	8.174

Table 5. Hausdorff dimensions estimated by power function method, Hurst exponents, standard deviations, average deviations and directional *JRCs* of samples C, D. Averaged values on these quantities are in the second last row, corresponding values of $3D$ surface are in the last row.

| Angle	Sample C						Sample D					
	Dim	Hurst	σ	ρ	JRC_σ	JRC_ρ	Dim	Hurst	σ	ρ	JRC_σ	JRC_ρ
0°	1.318	0.682	3.994	4.156	13.149	12.306	1.087	0.913	2.765	3.232	8.579	8.852
10°	1.459	0.541	3.319	3.689	13.564	13.185	1.109	0.891	3.404	3.933	9.970	10.119
20°	1.494	0.506	2.909	3.495	12.992	13.275	1.161	0.839	3.511	4.508	10.578	11.403
30°	1.455	0.545	3.500	3.411	13.968	12.514	1.157	0.843	3.517	4.607	10.555	11.518
40°	1.401	0.599	3.888	4.073	14.063	13.158	1.156	0.844	4.151	4.693	11.743	11.640
50°	1.372	0.628	4.749	4.507	15.526	13.598	1.150	0.850	4.427	4.776	12.192	11.718
60°	1.399	0.601	4.283	4.656	14.945	14.246	1.117	0.883	4.449	4.821	11.932	11.514
70°	1.346	0.654	4.284	4.504	14.137	13.253	1.116	0.884	4.057	4.713	11.232	11.349
80°	1.293	0.707	4.260	4.166	13.402	12.064	1.105	0.895	3.730	4.286	10.549	10.631
90°	1.415	0.585	3.120	3.356	12.385	11.872	1.132	0.868	2.953	3.397	9.248	9.406
100°	1.481	0.519	2.142	2.488	10.491	10.645	1.094	0.906	4.227	4.147	11.351	10.346
110°	1.385	0.615	1.939	2.104	8.809	8.670	1.086	0.914	5.082	4.872	12.721	11.350
120°	1.396	0.604	1.865	1.846	8.689	8.099	1.103	0.897	5.948	6.555	14.253	13.741
130°	1.419	0.581	1.783	1.809	8.656	8.190	1.047	0.953	7.430	10.987	15.831	18.124
140°	1.474	0.526	1.609	1.819	8.636	8.729	1.142	0.858	8.048	11.253	17.850	19.603
150°	1.398	0.602	1.705	1.797	8.220	7.986	1.059	0.941	9.160	12.247	18.281	19.509
160°	1.338	0.662	2.288	2.540	9.345	9.295	1.062	0.938	8.338	10.554	17.234	17.857
170°	1.357	0.643	2.630	2.903	10.420	10.256	1.061	0.939	6.999	8.614	15.376	15.776
180°	1.270	0.730	3.976	4.447	12.550	12.307	1.050	0.950	5.728	7.242	13.408	14.104
190°	1.279	0.721	4.487	4.769	13.679	12.933	1.082	0.918	6.110	6.520	14.293	13.510
200°	1.256	0.744	3.871	3.862	12.179	11.164	1.076	0.924	6.594	7.103	14.948	14.170
210°	1.341	0.659	2.901	2.715	10.938	9.709	1.104	0.896	7.429	9.604	16.480	17.344
220°	1.389	0.611	2.006	1.724	9.038	7.712	1.044	0.956	9.084	12.200	17.998	19.277
230°	1.464	0.536	1.476	1.475	8.069	7.599	1.059	0.941	9.968	12.504	19.312	19.758
240°	1.293	0.707	2.257	2.359	8.878	8.539	1.047	0.953	9.273	12.537	18.282	19.641
250°	1.359	0.641	2.206	2.253	9.322	8.813	1.061	0.939	6.954	7.819	15.318	14.881
260°	1.299	0.701	2.556	3.251	9.680	10.432	1.126	0.874	4.916	4.973	12.810	11.803
270°	1.258	0.742	2.704	3.393	9.675	10.343	1.156	0.844	3.479	2.549	10.476	8.038
280°	1.269	0.731	3.062	3.612	10.589	10.841	1.168	0.832	2.007	1.992	7.402	6.981
290°	1.283	0.717	3.271	4.590	11.189	12.685	1.203	0.797	1.653	1.454	6.711	5.918
300°	1.229	0.771	4.576	6.858	13.262	15.480	1.223	0.777	2.021	2.052	7.771	7.407
310°	1.273	0.727	5.372	7.117	15.294	16.415	1.219	0.781	2.294	2.474	8.410	8.274
320°	1.255	0.745	5.775	7.138	15.770	16.198	1.131	0.869	2.798	3.073	8.924	8.845
330°	1.224	0.776	5.668	6.636	15.178	15.120	1.154	0.846	2.435	2.700	8.303	8.315
340°	1.298	0.702	4.931	5.576	14.793	14.452	1.111	0.889	2.514	2.735	8.205	8.128
350°	1.376	0.624	4.124	4.400	14.221	13.445	1.089	0.911	2.406	2.584	7.849	7.736
Aver.	1.350	0.650	3.319	3.708	11.825	11.542	1.112	0.888	4.996	5.953	12.399	12.461
3D	2.398	0.602	3.356	3.612	12.739	12.193	2.081	0.919	5.144	5.487	12.775	12.159
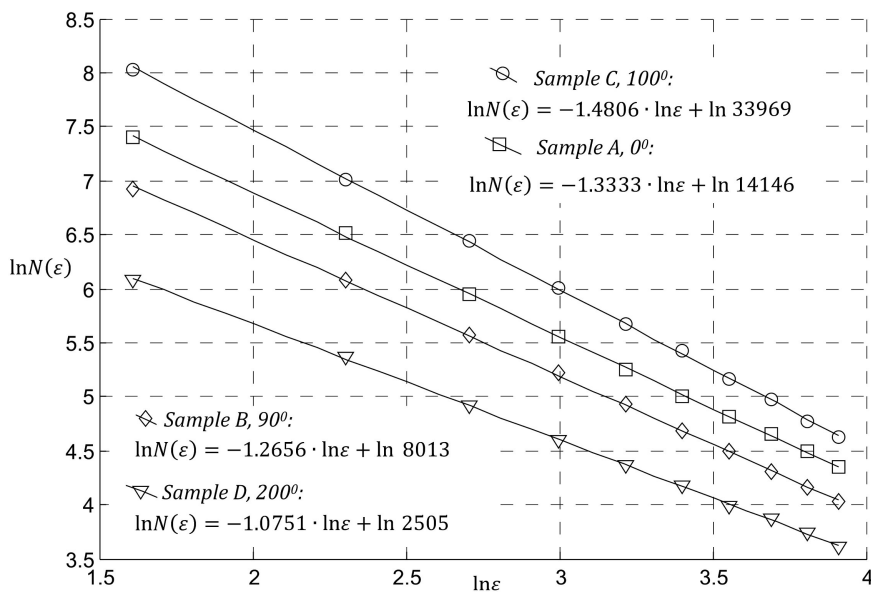
Figure 14. Graphical representation of profile dimension estimation: sample A, direction $0°$, sample B, direction $90°$, sample C direction $100°$, sample D, direction $200°$ (box counting method).
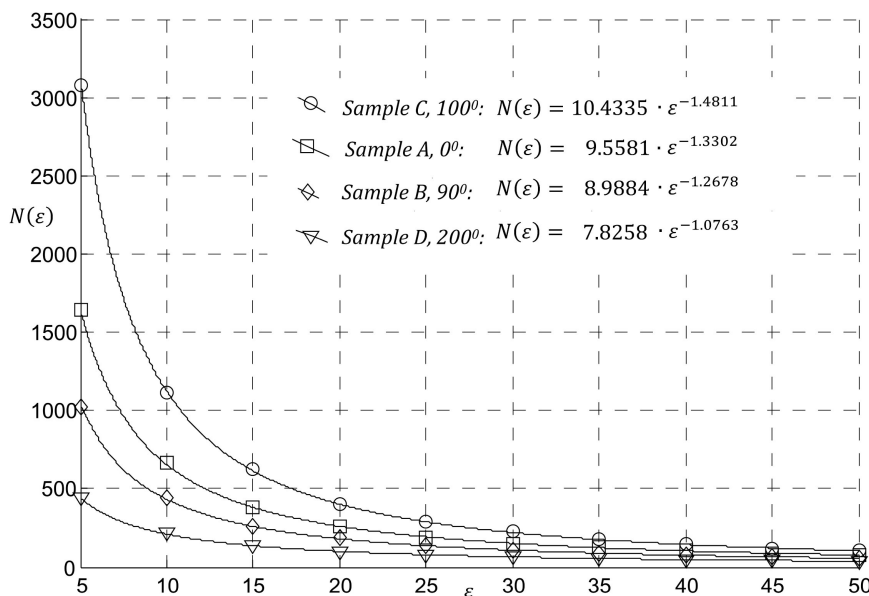
Figure 15. Graphical representation of profile dimension estimation: sample A, direction $0°$, sample B, direction $90°$, sample C direction $100°$, sample D, direction $200°$ (power function method).

1) Directional JRC_σ is marked as red solid

2) Directional JRC_ρ is marked as green solid

3) Average of directional JRC_σ is marked as red dashed

4) Average of directional JRC_ρ is marked as green dashed

5) Global JRC_σ is marked as blue

6) Global JRC_ρ is marked as dark pink
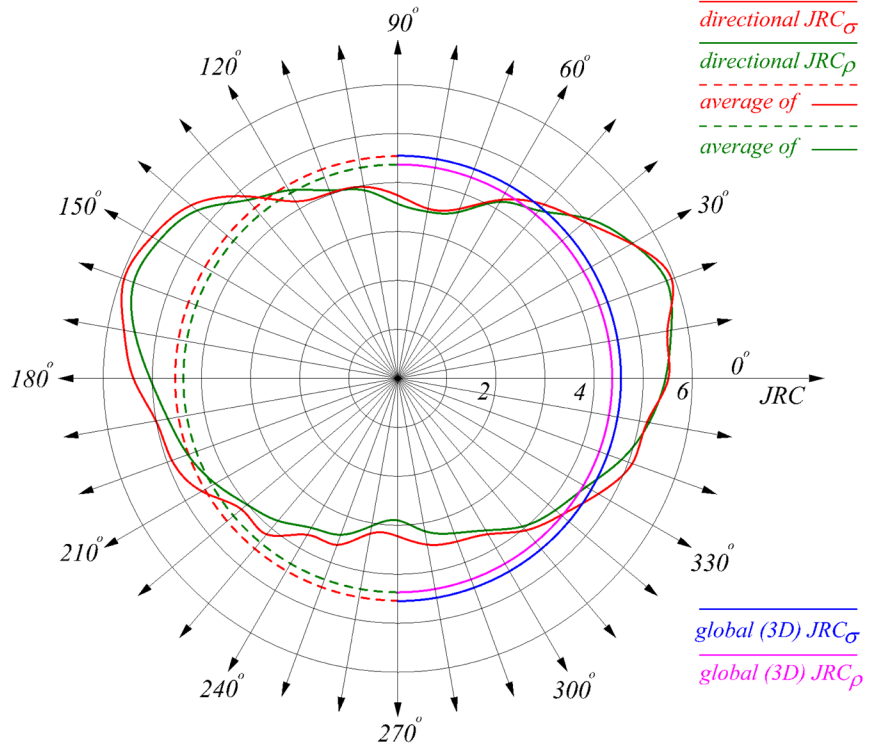
Figure 16. Directional JRC_σ and JRC_ρ, average of directional JRC_σ and JRC_ρ, global (3) JRC_σ and JRC_ρ of the sample A.
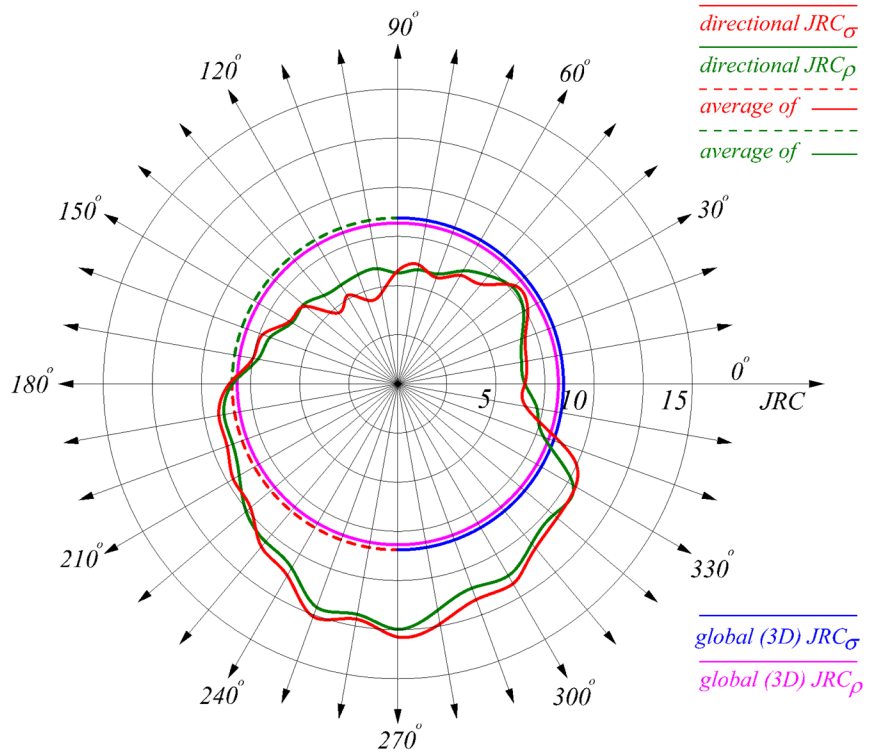
Figure 17. Directional JRC_σ and JRC_ρ, average of directional JRC_σ and JRC_ρ, global ($3D$) JRC_σ and JRC_ρ of the sample B.
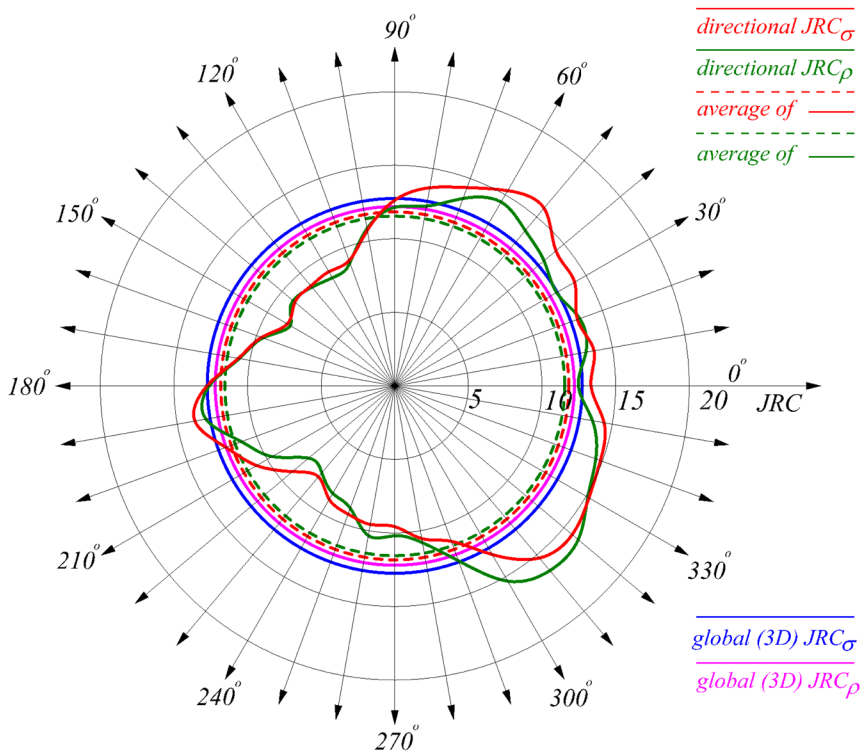
Figure 18. Directional JRC_σ and JRC_ρ, average of directional JRC_σ and JRC_ρ, global ($3D$) JRC_σ and JRC_ρ of the sample C.
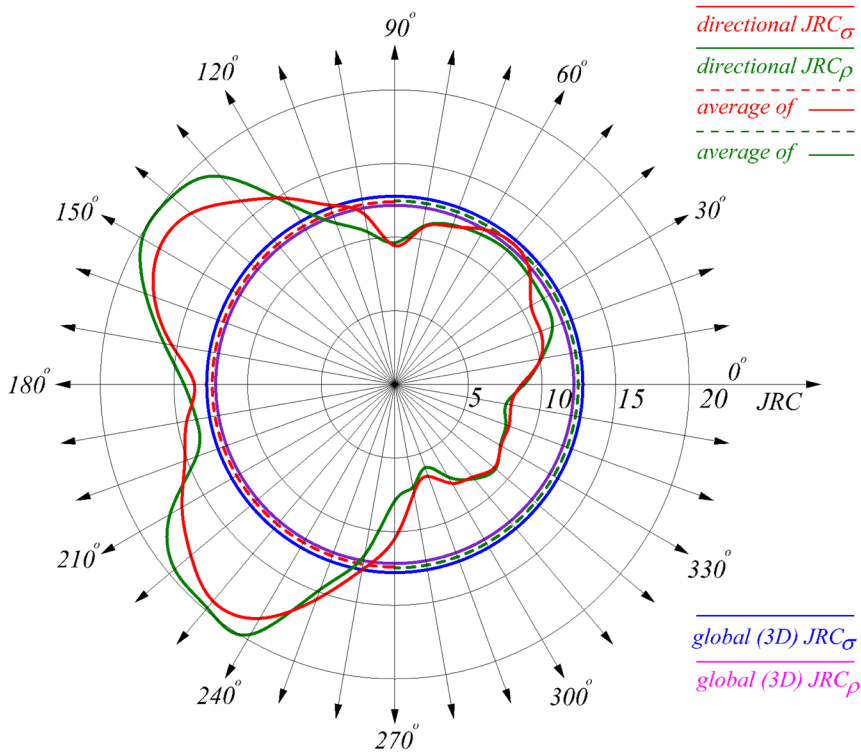
Figure 19. Directional JRC_σ and JRC_ρ, average of the directional JRC_σ and JRC_ρ, global ($3D$) JRC_σ and JRC_ρ of the sample D.

11. Conclusions

This article showed that the fractal dimension does not dependent on scaling. Therefore, there exists no direct relationship between the fractal dimension and *JRC*, any fractal dimension itself cannot be used for roughness modelling. *JRC* depends not only on the fractal dimension, but also on other variables. In this paper, statistical variability of the surface has been used. Increasing irregularities heights denote increasing of the *JRC* and conversely. Therefore, the standard deviation or average deviation must be placed to numerator of the *JRC* estimator.

The *JRC* estimator is designed to be able to determine the *JRC* in different topological dimensions, *i.e.* the *JRC* of fractal curves and the *JRC* of fractal surfaces as well. Therefore, Hurst exponent was used instead the fractal dimension. Increasing dimension denotes increasing roughness and decreasing Hurst exponent. Conversely-decreasing dimension denotes decreasing roughness and increasing Hurst exponent. For this reason, Hurst exponent must be placed to denominator of the *JRC* is estimator.

The estimator enables fully automatic estimation of the isotropic (global) joint roughness coefficient (this assumes independence on the direction) and also anisotropic (directional) joint roughness coefficient (which value depends on the direction). In case of the isotropic *JRC*, the estimator works with whole surface which is topologically two-dimensional, in case of the anisotropic *JRC*, the estimator works in chosen direction, *i.e.* with topologically one-dimensional profile. The average of the anisotropic *JRC* estimated for 360˚ with step 10˚ is approximately equal to the isotropic (global) *JRC*.

Acknowledgements

References

[1] Barton, N. and Choubey, V. (1977): The Shear Strength of Rock Joints in Theory and Practice. *Rock Mechanics*, **10**, 1-65. https://doi.org/10.1007/BF01261801

[2] Tse, R. and Cruden, D.M. (1979) Estimating Joint Roughness Coefficients. *International Journal of Rock Mechanics and Mining Sciences*, **16**, 303-307. https://doi.org/10.1016/0148-9062(79)90241-9

[3] Maerz, N.H., Franklin, J.A., and Bennett, C.P. (1990) Joint Roughness Measurement Using Shadow Profilometry. *International Journal of Rock Mechanics and Mining Sciences*, **27**, 329-343. https://doi.org/10.1016/0148-9062(90)92708-M

[4] Hong, E.-S., Lee, I.-M. and Lee, J.-S. (2006) Measurement of Rock Joint Roughness by 3D Scanner. *Geotechnical Testing Journal*, **29**, 1-8.

[5] Hong, E.-S., Lee, I.-M. and Lee, J.-S. (2008) Underestimation of Roughness in

Rough Rock Joints. *International Journal for Numerical and Analytical Methods in Geomechanics*, **32**, 1385-1403. https://doi.org/10.1002/nag.678

[6]   Fardin, N., Stephansson, O. and Jing, L. (2001) The Scale Dependence of Rock Joint Surface Roughness. *International Journal of Rock Mechanics and Mining Sciences*, **38**, 659-669. https://doi.org/10.1016/S1365-1609(01)00028-4

[7]   Brown, S.R. and Scholz, C.H. (1985) Broad Band Width Study of the Topography of Natural Rock Surfaces. *Journal of Geophysics Research*, **90**, 12575-12582. https://doi.org/10.1029/JB090iB14p12575

[8]   Miller, S.M., McWilliams, P.C. and Kerkering, J.C. (1990) Ambiguities in Estimating Fractal Dimensions of Rock Fracture Surfaces. In: Balkema, A.A., Ed., *Proceedings of the* 31*st U.S. Symposium, Colorado School of Mines*, Rotterdam, June 18-20 1990, 471-478.

[9]   Power, W.L. and Tullis, T.E. (1991) Euclidean and Fractal Models for the Description of Rock Surface Roughness. *Journal of Geophysical Research*, **96**, 415-424. https://doi.org/10.1029/90JB02107

[10] Huang, S.L., Oelfke, S.M. and Speck, R.C. (1992) Applicability of Fractal Characterization and Modeling to Rock Joint Profiles. *International Journal of Rock Mechanics and Mining Science*, **29**, 89-98. https://doi.org/10.1016/0148-9062(92)92120-2

[11] Poon, C.Y., Sayles, R.S. and Jones, T.A. (1992) Surface Measurement and Fractal Characterization of Naturally Fractured Rocks. *Journal of Physics D: Applied Physics*, **25**, 1269-1275. https://doi.org/10.1088/0022-3727/25/8/019

[12] Odling, N.E. (1994) Natural Fracture Profiles, Fractal Dimension and Joint Roughness Coefficients. *Rock Mechanics*, **27**, 135-153. https://doi.org/10.1007/BF01020307

[13] Den Outer, A., Kaashoek, J.F. and Hack, H.R.G.K. (1995) Difficulties with Using Continuous Fractal Theory for Discontinuity Surfaces. *International Journal of Rock Mechanics and Mining Science*, **32**, 3-10. https://doi.org/10.1016/0148-9062(94)00025-X

[14] Ficker, T. (2016) Fractal Properties of Rock Joint Coefficients. *International Journal of Rock Mechanics & Mining Science*, **94**, 27-31. https://doi.org/10.1016/j.ijrmms.2017.02.014

[15] Lee, Y.H., Carr, J.R., Barr, D.J. and Haas, C.J. (1990) The Fractal Dimension as a Measure of the Roughness of Rock Discontinuity Profiles. *International Journal of Rock Mechanics and Mining Sciences*, **27**, 453-464. https://doi.org/10.1016/0148-9062(90)90998-H

[16] Li, Y. and Huang, R. (2015) Relationship between Joint Roughness Coefficient and Fractal Dimension of Rock Fracture Surfaces. *International Journal of Rock Mechanics and Mining Sciences*, **75**, 15-22. https://doi.org/10.1016/j.ijrmms.2015.01.007

[17] Sanei, M., Faramarzi, L., Goli, S., *et al.* (2015) Development of a New Equation for Joint Roughness Coefficient (JRC) with Fractal Dimension: A Case Study of Bakhtiary Dam Site in Iran. *Arabian Journal of Geosciencies*, **8**, 465-475. https://doi.org/10.1007/s12517-013-1147-3

[18] Li, Y., Oh, J., Mitra, R., *et al.* (2017) A Fractal Model for the Shear Behaviour of Large-Scale Opened Rock Joints. *Rock Mechanics and Rock Engineering*, **50**, 67-79. https://doi.org/10.1007/s00603-016-1088-8

[19] Gneiting, T. and Schlather, M. (2004) Stochastic Models Which Separate Fractal Dimension and Hurst Effect. Cornell University Library. *SIAM Review*, **46**, 269-282.

https://doi.org/10.1137/S0036144501394387

[20] Feder, J. (1988) Fractals. Plenum Press, New York.

[21] Maliverno, A. (1990) A Simple Method to Estimate Fractal Dimension of a Self-Affine Series. *Geophysical Research Letters*, **17**, 1953-1956. https://doi.org/10.1029/GL017i011p01953

[22] Bovil, C. (1996) Fractal Geometry in Architecture and Design. Birkhäuser, Boston. https://doi.org/10.1007/978-1-4612-0843-3

[23] Stamps, A.E. (2002) Fractals, Skylines, Nature and Beauty. *Landscape and Urban Planning*, **60**, 163-184. https://doi.org/10.1016/S0169-2046(02)00054-3

[24] Mandelbrot, B.B. (1967) How Long Is the Coast of Britain? Statistical Self-Similarity and Fractional Dimension. *Science*, **156**, 636-638. https://doi.org/10.1126/science.156.3775.636

[25] Hastings, H. and Sugihara, G. (1993) Fractals—A User's Guide for the Natural Sciences. Oxford University Press, Oxford.

[26] Martišek, D. and Druckmüllerová, H. (2014) Power-Function Method of Fractal Dimension Estimation. *20th International Conference of Soft Computing Mendel* Brno, 26-27 June 2014, 147-152.

[27] Kulatilake, P.H.S.W., *et al.* (2006) Natural Rock Joint Roughness Quantification through Fractal Techniques. *Geotechnical and Geological Engineering*, **24**, 1181-1202. https://doi.org/10.1007/s10706-005-1219-6

[28] Power, W.L. and Tullis, T.E. (1991) Euclidean and Fractal Models for the Description of Rock Surface Roughness. *Journal of Geophysical Research*, **96**, 415-424. https://doi.org/10.1029/90JB02107

[29] Brown, S.R. (1987) A Note on the Description of Surface Roughness Using Fractal Dimension. *Geophysical Research Letters*, **14**, 1095-1098. https://doi.org/10.1029/GL014i011p01095

[30] Brown, S.R. (1995) Simple Mathematical Model of a Rough Fracture. *Journal of Geophysical Research*, **100**, 5941-5952. https://doi.org/10.1029/94JB03262

[31] Mandelborot, B. (1982) The Fractal Geometry of Nature. W. H. Freeman, San Francisco.

[32] Turcotte, D.L. (1992) Fractals and Chaos in Geology and Geophysics. Cambridge University Press, Cambridge.

[33] Martišek, D. (2002) The 2-D and 3-D Processing of Images Provided by Conventional Microscopes. *Scanning*, **24**, 284-296. https://doi.org/10.1029/94JB03262

[34] Martišek, D. and Druckmüllerová, H. (2014a) Multifocal Image Processing. *Mathematics for Applications*, **3**, 77-90. https://doi.org/10.13164/ma.2014.06

[35] Martišek, D., *et al.* (2015) High-Quality Three-Dimensional Reconstruction and Noise Reduction of Multifocal Images from Oversized Samples. *Journal of Electronic Imaging*, **24**, Article ID: 053029. https://doi.org/10.1117/1.JEI.24.5.053029

[36] Martišek, D. and Druckmüllerová, H. (2017) Registration of Partially Focused Images for 2D and 3D Reconstruction of Oversized Samples. *Scanning*, **2017**, Article ID: 8538215, 8 p.